

Magnon transport in $Y_3Fe_5O_{12}/Pt$ nanostructures with reduced effective magnetizationJ. Gückelhorn ^{1,2,*} T. Wimmer,^{1,2} M. Müller ^{1,2} S. Geprägs ¹ H. Huebl ^{1,2,3} R. Gross ^{1,2,3} and M. Althammer ^{1,2,†}¹Walther-Meißner-Institut, Bayerische Akademie der Wissenschaften, 85748 Garching, Germany²Physik-Department, Technische Universität München, 85748 Garching, Germany³Munich Center for Quantum Science and Technology (MCQST), D-80799 München, Germany

(Received 23 July 2021; revised 5 November 2021; accepted 5 November 2021; published 29 November 2021)

For applications making use of magnonic spin currents damping effects, which decrease the spin conductivity, have to be minimized. We here investigate the magnon transport in a yttrium iron garnet thin film with strongly reduced effective magnetization. We show that in a three-terminal device the effective magnon conductivity can be increased by a factor of up to six by a current applied to a modulator electrode, which generates damping compensation above a threshold current. Moreover, we find a linear dependence of this threshold current on the applied magnetic field. We can explain this behavior by the reduced effective magnetization and the associated nearly circular magnetization precession.

DOI: [10.1103/PhysRevB.104.L180410](https://doi.org/10.1103/PhysRevB.104.L180410)

Pure spin currents carried by magnons, the elementary excitations of the spin system in magnetically ordered insulators (MOIs), have drawn much attention due to their potential applications in information processing at a low dissipation level [1–4]. The MOI yttrium iron garnet ($Y_3Fe_5O_{12}$, YIG) is a promising candidate for hosting efficient magnon based spin transport due to its low Gilbert damping parameter even in nanometer-thin films [5] and its correspondingly large magnon propagation length [6–9]. Amongst the device concepts enabling logic operation with magnonic spin currents, transistor-inspired devices and even logic gates have been demonstrated [4,10–13]. Such transistor-like device concepts generally rely on spin-transfer torque for spin current generation. The latter can be realized in bilayers consisting of MOIs and heavy metals with strong spin-orbit coupling via the spin Hall effect (SHE) [7,14–21]. The magnon transport in the MOI can be controlled via an electrical charge current, and the resulting effect is typically represented by a change in the effective magnon conductivity [4,10]. At a certain threshold current the injected magnons can even counteract the magnetization damping, which results in an abrupt increase of the effective magnon conductivity. The present understanding is that this threshold effect scales with the saturation magnetization M_s and the magnetic anisotropy of the materials [10,22]. This warrants to explore the impact of these parameters on controlling the magnon conductivity in MOIs, which has not been pursued so far to the best of our knowledge.

In this Letter, we investigate the diffusive magnon transport in MOIs with significant perpendicular magnetic anisotropy fields H_k and reduced M_s . To this end, we biaxially strain the YIG thin film hosting the magnons by growing YIG on yttrium scandium gallium garnet ($Y_3Sc_2Ga_3O_{12}$, YSGG). Our films exhibit low Gilbert damping comparable to YIG thin films grown on lattice-matched substrates. By investigating the magnon transport in three-terminal devices, we find that

the threshold current, which defines the onset of the regime with compensated damping, depends linearly on the applied magnetic field. Moreover, we can corroborate the expected scaling with the effective magnetization of the MOI.

Our experimental approach utilized to enhance the magnon-based spin conductivity is based on the minimization of the ellipticity of the magnetization precession. As sketched in Fig. 1(a), YIG thin films grown on the lattice-matched substrate gadolinium gallium garnet ($Gd_3Ga_5O_{12}$, GGG) exhibit a finite in-plane effective magnetization $M_{\text{eff}} = M_s - H_k > 0$, and thus an elliptical magnetization precession trajectory with the long axis aligned in the film plane, giving rise to nonlinear damping effects via parametric pumping of higher frequency magnon modes [23]. Recent experiments reported the minimization of the ellipticity of the magnetization precession (approaching $M_{\text{eff}} = 0$) and thereby achieved spin-orbit torque induced coherent magnetization auto-oscillations even in extended magnetic films [24,25]. For our experiments, we also reduce the ellipticity of the magnetization precession by reducing the effective magnetization of YIG. Approaching a compensation of the anisotropy ($M_{\text{eff}} = 0$), a circular magnetization precession is expected and, hence, nonlinear damping effects should be suppressed [cf. Fig. 1(b)]. To be able to control M_{eff} , we biaxially strain the $t_{\text{YIG}} = 12.3$ nm thick YIG film by growing it pseudomorphically onto an YSGG substrate by pulsed laser deposition (see Ref. [26] for growth details). The lattice mismatch of 0.4 % between YIG and YSGG induces a biaxial in-plane tensile strain in the YIG thin film. This strain can result in a strong H_k [27], originating from the strain-induced magnetoelastic coupling [28]. Figure 1(c) shows the $2\theta - \omega$ x-ray diffraction scan of the thin film confirming the in-plane lattice strain. The substrate (444) diffraction peak is clearly visible at $2\theta = 50.7^\circ$, while the corresponding broad film peak is shifted to larger 2θ values due to the tensile strain and appears as a shoulder in the diffraction pattern. Note, that the large width and low intensity of the film peak is due to the small film thickness. We magnetically characterize the strained YIG film using broadband ferromagnetic

*janine.gueckelhorn@wmi.badw.de

†matthias.althammer@wmi.badw.de

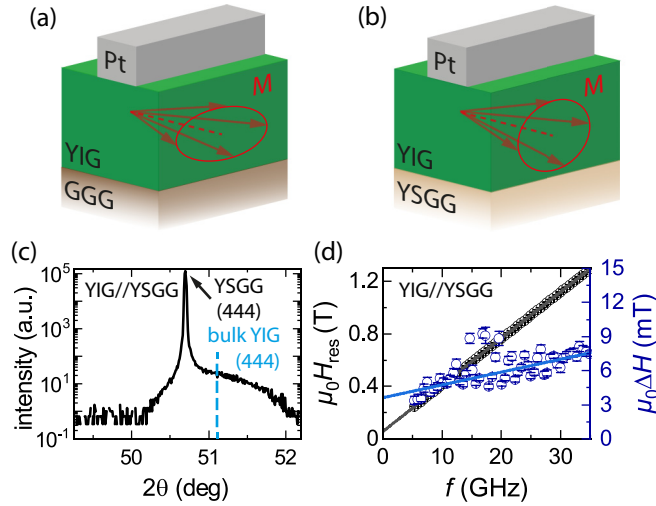


FIG. 1. (a) Sketch of the ellipticity of the magnetization precession in YIG thin films grown on lattice-matched GGG. (b) In biaxially strained YIG thin films grown on YSGG, the ellipticity is minimized due to the reduced effective magnetization. (c) X-ray diffraction of a 12.3 nm thick YIG film grown on a (111)-oriented YSGG substrate. The blue vertical line marks the calculated 2θ -position of the (444) reflection of bulk YIG. (d) Resonance field H_{res} and linewidth ΔH extracted from FMR measurements of the YIG film on YSGG as a function of frequency. Via a Kittel fit (gray line) we extract $\mu_0 M_{\text{eff}} = 56 \pm 0.2$ mT and from a linear fit to the linewidth (blue line) we obtain $\mu_0 \delta H = (3.6 \pm 0.4)$ mT and $\alpha_G = (1.5 \pm 0.2) \times 10^{-3}$.

resonance (FMR) as shown in Fig. 1(d). We determine the effective magnetization $\mu_0 M_{\text{eff}} = 56 \pm 0.2$ mT of the thin film by extracting the resonance field $\mu_0 H_{\text{res}}$ applied in the out-of-plane direction as a function of the stimulus frequency of the microwave radiation and linear fitting with the Kittel equation. This value is about three times smaller compared to unstrained YIG films of similar thickness [10]. Moreover, FMR enables us to determine the Gilbert damping parameter α_G [see Fig. 1(d)] [29]. By fitting the FMR linewidth ΔH to $\mu_0 \Delta H = \mu_0 \delta H + 4\pi f \alpha_G / \gamma$ (blue line) with $\gamma = \frac{g\mu_B}{\hbar}$ the gyromagnetic ratio with the Landé factor g and Bohr's magneton μ_B , we obtain the inhomogeneous FMR linewidth $\mu_0 \delta H = (3.6 \pm 0.4)$ mT and $\alpha_G = (1.5 \pm 0.2) \times 10^{-3}$. Similar values for α_G were obtained for an epitaxial high-quality YIG film grown on lattice-matched GGG under the same conditions [10].

As a next step, we deposit *ex situ* 5-nm-thick Pt strips on top of the strained YIG film using electron beam lithography and magnetron sputtering, allowing for an all-electrical generation and detection of pure spin currents [4]. With this sample, we investigate diffusive magnon transport using twin-strip structures as depicted in Fig. 2(a). In our experiments a DC charge current $I^{\text{inj}} = 100 \mu\text{A}$ is fed through one Pt strip (injector) to inject magnons into the YIG via the SHE. The magnons diffuse away from the injector and can then be electrically detected via the inverse SHE at the second Pt strip (detector) as a voltage signal V^{det} . In our sample an injector width of $w_{\text{inj}} = 500$ nm is used, while the detector width w_{det} and the center-to-center distance d_c between injector and detector is varied. Using a current reversal technique we unambiguously

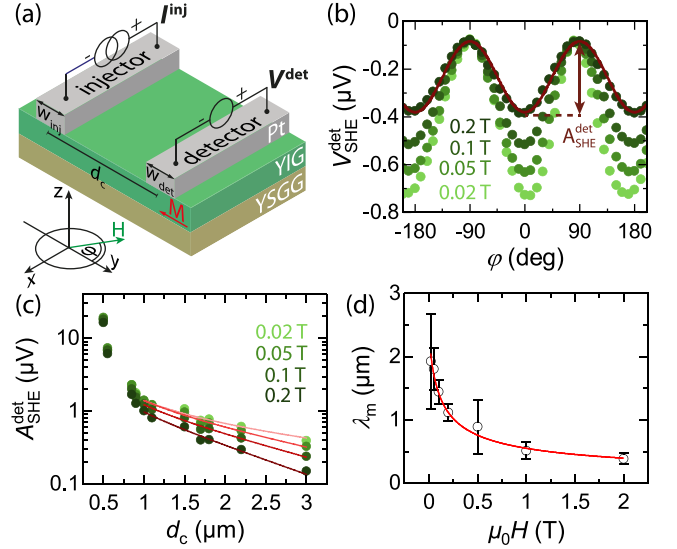


FIG. 2. (a) Sketch of the sample configuration with the electrical connection scheme, and the coordinate system with the in-plane rotation angle φ of the applied magnetic field $\mu_0 \mathbf{H}$. (b) Detector signal $V_{\text{SHE}}^{\text{det}}$ plotted versus the magnetic field orientation φ for different magnetic field magnitudes $\mu_0 H$. The red line is a fit to $A_{\text{SHE}}^{\text{det}} \cos^2(\varphi)$. (c) The voltage amplitudes $A_{\text{SHE}}^{\text{det}}$, as indicated in (b), plotted versus the distance d_c for different magnetic fields on a logarithmic scale. The red lines correspond to exponential fits to the data points for $d_c \geq 1 \mu\text{m}$. (d) Extracted magnon spin diffusion lengths λ_m from the exponential fits in (c) for different magnetic field magnitudes $\mu_0 H$. The red line is a fit to Eq. (2), resulting in a magnon diffusion constant $D = (1.75 \pm 0.05) \times 10^{-4} \text{ m}^2/\text{s}$.

can assign the measured detector voltage $V_{\text{SHE}}^{\text{det}}$ to the magnons generated at the injector via the SHE [13,16]. To characterize the magnon transport, we measure the voltage signal $V_{\text{SHE}}^{\text{det}}$ as a function of the magnetic field orientation φ [cf. Fig. 2(a)] with fixed magnitude $\mu_0 H$ at a temperature of 280 K. The data are shown in Fig. 2(b) for $d_c = 2.2 \mu\text{m}$ and $w_{\text{det}} = 500$ nm. The results show the distinctive $\cos^2(\varphi)$ angular variation expected for diffusive transport of SHE-generated magnons from injector to detector [4,16]. The angle dependence can be fitted with a simple $A_{\text{SHE}}^{\text{det}} \cos^2(\varphi)$ function, as exemplary shown for $\mu_0 H = 200$ mT, where $A_{\text{SHE}}^{\text{det}}$ corresponds to the amplitude of the SHE-induced magnon transport signal. The quantity $A_{\text{SHE}}^{\text{det}}$ is plotted in Fig. 2(c) as a function of d_c for different $\mu_0 H$. We observe a decrease of $A_{\text{SHE}}^{\text{det}}$ with increasing d_c as expected for diffusive magnon transport: at distances shorter than the magnon diffusion length λ_m , $A_{\text{SHE}}^{\text{det}}$ follows a $1/d_c$ dependence, while for larger distances the magnon relaxation dominates and an exponential decay is observed [7,19]. An exponential fit to the data measured for $d_c > 1 \mu\text{m}$ (red lines), allows us to extract λ_m . The extracted values are shown in Fig. 2(d) as a function of the magnetic field magnitude $\mu_0 H$. The λ_m values are of the order of $1 \mu\text{m}$ and thus in good agreement with the values found for YIG films grown on lattice-matched GGG [10]. To discuss the physics leading to the magnetic field dependence of λ_m in more detail, we consider the magnon relaxation rate $\Gamma_{\text{mr}}^{\text{ip}}$, which is given by

$$\Gamma_{\text{mr}}^{\text{ip}} = \left(\alpha_G + \frac{\delta H}{2\sqrt{H(H + M_{\text{eff}})}} \right) \gamma \mu_0 \left(H + \frac{M_{\text{eff}}}{2} \right) \quad (1)$$

for an in-plane magnetized film [30]. Taking damping contributions from inhomogeneous broadening δH into account [31], the damping rate Γ_{mr}^{ip} diverges for a finite positive M_{eff} at $\mu_0 H = 0$. However, in the limit of $M_{eff} = 0$, the relaxation rate is constant for $\mu_0 H = 0$ and we expect a strictly linear dependence on the magnetic field. Together with $\lambda_m = \sqrt{D\tau_m}$ and $\tau_m = 1/\Gamma_{mr}^{ip}$ with D the magnon diffusion constant and τ_m the magnon lifetime, we can describe the magnetic field dependence of λ_m determined from the twin-strip transport measurements as

$$\lambda_m = \sqrt{\frac{D}{\gamma\mu_0(\alpha_G H + \frac{\delta H}{2})}}. \quad (2)$$

As shown in Fig. 2(d), the experimental data can be well fitted by Eq. (2). Utilizing the values obtained from the FMR measurements and neglecting the field dependence of D , we obtain a magnon diffusion constant of $D = (1.75 \pm 0.05) \times 10^{-4} \text{ m}^2/\text{s}$. Similar values were obtained for YIG films on GGG, supporting the quantitative understanding of the phenomenon [32].

Next, we turn to three-terminal devices, which allow us to manipulate the magnon transport between injector and detector via the center Pt strip acting as modulator [see Fig. 3(a)]. In this configuration, we apply a low-frequency (7 Hz) charge current $I_{ac}^{inj} = 200 \mu\text{A}$ to the injector strip, while a constant DC charge current I_{dc}^{mod} is applied to the modulator strip. The detector voltage V^{det} is recorded via lock-in detection, where the first harmonic voltage signal $V_{1\omega}^{det}$ can be assigned to the transport of magnons generated via the SHE at the injector. This AC readout technique is essential to distinguish between the magnons generated by the DC driven modulator and the AC driven injector. Therefore any change in the first harmonic signal $V_{1\omega}^{det}$ reflects a change in the magnon conductivity. We measure $V_{1\omega}^{det}$ as a function of the magnetic field orientation φ for different external magnetic field magnitudes and different modulator currents I_{dc}^{mod} . Typical results for a structure with an edge-to-edge distance $d_e = 200 \text{ nm}$ and a modulator width $w_{mod} = 400 \text{ nm}$, while $w_{inj} = w_{det} = 500 \text{ nm}$ and $\mu_0 H = 50 \text{ mT}$, are plotted in Fig. 3(b). For $I_{dc}^{mod} = 0$ (black data points), $V_{1\omega}^{det}$ exhibits the same $\cos^2(\varphi)$ variation as in our twin-strip structures [4,16]. As reported previously [10,11], we observe a significant enhancement of $V_{1\omega}^{det}$ at $\varphi = \pm 180^\circ$ for $I_{dc}^{mod} > 0$. This observation can be attributed to a magnon accumulation underneath the modulator caused by the SHE-induced magnon chemical potential and thermally generated magnons due to Joule heating. This accumulation increases the magnon conductivity, resulting in a larger voltage signal $V_{1\omega}^{det}$. At $\varphi = 0^\circ$, the magnon transport signal is slightly suppressed, originating from the nearly compensation of the magnon depletion caused by the SHE by thermally generated magnons. For $I_{dc}^{mod} < 0$, we observe a 180° shifted angle dependence of the detector voltage signal, i.e. an increase at $\varphi = 0^\circ$ and a reduction at $\varphi = \pm 180^\circ$. This behavior is fully consistent with the assumption that there are both SHE and Joule heating contributions [4,10,11]. For a more quantitative analysis, we extract the signal amplitudes $A_{1\omega}^{det}(+\mu_0 H)$ at $\varphi = 180^\circ$ and $A_{1\omega}^{det}(-\mu_0 H)$ at $\varphi = 0^\circ$ and plot them as a function of the modulator current I_{dc}^{mod} for different $\mu_0 H$ in Fig. 3(c). For $|I_{dc}^{mod}| < 0.25 \text{ mA}$, we observe the expected superposition of a

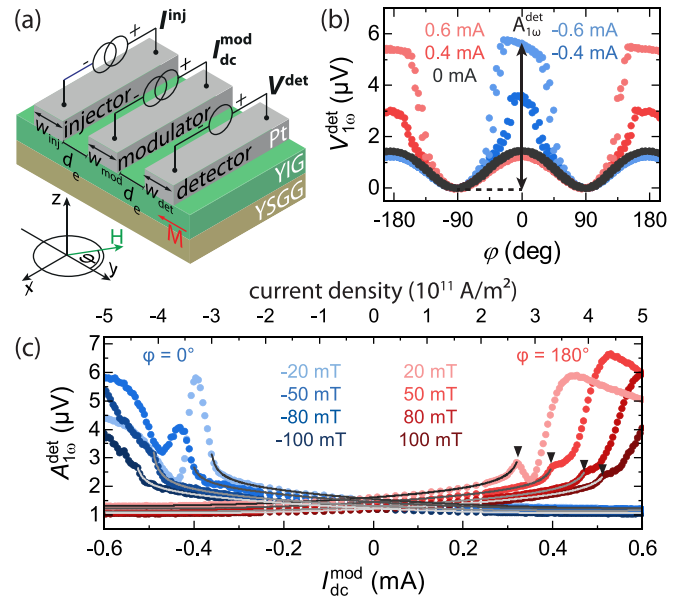


FIG. 3. (a) Sketch of the sample configuration for a three-terminal device with the electrical connection scheme, and the coordinate system with the in-plane rotation angle φ of the applied magnetic field $\mu_0 \mathbf{H}$. (b) Detector signal $V_{1\omega}^{det}$ of a structure with $d_e = 200 \text{ nm}$ and $w_{mod} = 400 \text{ nm}$ plotted versus the magnetic field orientation with constant magnitude $\mu_0 H = 50 \text{ mT}$ for various modulator currents I_{dc}^{mod} . (c) The voltage amplitudes $A_{1\omega}^{det}$, as indicated in (b), versus the DC charge current I_{dc}^{mod} . The gray lines indicate fits to Eq. (3) for current values below the threshold current.

linear and quadratic I_{dc}^{mod} dependence corresponding to SHE induced magnons and thermally generated magnons due to Joule heating, respectively [4,10,11]. However, for larger I_{dc}^{mod} a clear deviation from this behavior is observed. In particular, we observe a strongly increased signal amplitude $A_{1\omega}^{det}$. This observation can be attributed to an enhanced effective magnon conductivity underneath the modulator, which causes a strong increase of the detector signal at the same magnon injection rate at the injector. As reported previously [10], this enhanced magnon conductivity can be explained by the presence of a zero effective damping state generated below the modulator electrode via the SHE-mediated spin-orbit torque. We here observe a maximum enhancement of $A_{1\omega}^{det}$ by a factor of 6, a twofold increase as compared to our previous experiments. This strong enhancement can be attributed to the reduction in M_{eff} and the associated circular magnetization precession. In the nonlinear regime for $|I_{dc}^{mod}| > 0.25 \text{ mA}$, a rich peak structure is found. First onsets of such a peak structure have also been found in our previous work on unstrained YIG films grown on GGG [11]. In the theoretical work by Takei [33], a strong influence of fluctuations on the magnon conductivity has been predicted above the threshold for damping compensation, which causes instabilities also in the magnon conductivity in these three-strip devices. Micromagnetic simulations conducted for a similar device geometry indicated a strong chaotic behavior above the threshold current of damping compensation [34]. In experiments with metallic CoNi [25], a reduction of the magnon density was observed and attributed to nonlinear magnon damping effects as M_{eff} was

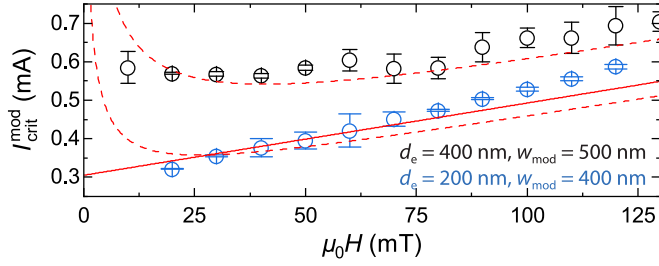


FIG. 4. Extracted critical currents $I_{\text{crit}}^{\text{mod}}$, as indicated by the black triangles in Fig. 3(c), as a function of the magnetic field magnitude μ_0H (blue circles). For comparison, the black data points are taken from our previous work, where we investigate an YIG thin film grown on lattice-matched GGG substrates [10]. The dashed lines correspond to fits to Eq. (4) with a finite M_{eff} , while the solid line is a fit to the data in the limit of $M_{\text{eff}} = 0$.

small but still finite in their case. For our sample, either nonlinear magnon damping processes due to a finite M_{eff} or instabilities in the magnon state caused by fluctuations may lead to the observed peak structure. However, more investigations are needed to unambiguously determine the physical origin of these peaks. Furthermore, we observe an asymmetry for the two magnetic field polarities in the amplitude signal $A_{1\omega}^{\text{det}}$. This is in stark contrast to the results obtained for YIG films on lattice-matched GGG [10,11]. At present, we can only speculate about the detailed origin of this asymmetry. It may be related to a combination of the following aspects: (i) a misalignment of the magnetic field due to trapped flux from our 3D-vector magnet, (ii) a Joule heating or electrical annealing, respectively, induced modification of the device properties, or (iii) effects related to the crystalline-orientation of YIG, such as a change in the magnetic anisotropy. The previously investigated YIG films were (001)-oriented [10], while here we use a (111) orientation allowing us to make use of the crystalline magnetic anisotropy.

The zero effective damping state and the corresponding peak-like structure in the magnon conductivity at the threshold value $I_{\text{crit}}^{\text{mod}}$ was recently discussed by S. Takei [33]. According to this model considerations, one can express the expected dependence of $A_{1\omega}^{\text{det}}$ originating from the thermal and SHE injection of magnons by

$$A_{1\omega}^{\text{det}}(I_{\text{dc}}^{\text{mod}}, \pm \mu_0H) = \frac{A + B\sqrt{1 \mp I_{\text{dc}}^{\text{mod}}/I_{\text{crit}}^{\text{mod}}}}{1 + C\sqrt{1 \mp I_{\text{dc}}^{\text{mod}}/I_{\text{crit}}^{\text{mod}}}}, \quad (3)$$

where the proportionality factors account for the induced magnon conductivity and A , B , C and $I_{\text{crit}}^{\text{mod}}$ are used as fit parameters. Note that the model is only valid up to $I_{\text{dc}}^{\text{mod}} = I_{\text{crit}}^{\text{mod}}$ and we thus restrict the fit with Eq. (3) to this region. The fit, indicated by gray lines in Fig. 3(c), reproduces well the measured data points. Although this model does not account for the amplitude asymmetry, it is well suited to extract the threshold current $I_{\text{crit}}^{\text{mod}}$.

For a quantitative comparison of the strained YIG films with reduced M_{eff} and conventional YIG thin films on GGG, we rely on the dependence of $I_{\text{crit}}^{\text{mod}}$ with μ_0H in Fig. 4. For the discussed structure (blue circles), we observe a linear increase of the critical current $I_{\text{crit}}^{\text{mod}}$ with applied magnetic

field for $\mu_0H > 20$ mT. This is in contrast to the observations in Ref. [10] (black circles), where an increase in $I_{\text{crit}}^{\text{mod}}$ with μ_0H is only observed for $\mu_0H > 50$ mT, while for $\mu_0H \leq 50$ mT $I_{\text{crit}}^{\text{mod}}$ remains constant. We note that $I_{\text{crit}}^{\text{mod}}$ versus μ_0H was associated with damping compensation [10]. Here, the spin injection rate due to SHE results in an interfacial spin transfer torque $\Gamma_{\text{ST}} \propto I_{\text{dc}}^{\text{mod}}$, which balances the intrinsic damping of the material. Hence, zero effective damping is achieved, when the condition $\Gamma_{\text{mr}}^{\text{ip}} = \Gamma_{\text{ST}}$ is satisfied [30]. In this regime, we can define the critical modulator current as [10]

$$I_{\text{crit}}^{\text{mod}} = \frac{\hbar \sigma_{\text{Pt}}}{e} \frac{t_{\text{Pt}} w_{\text{mod}}}{2l_s \theta_{\text{SH}} \tanh(\eta)} \left(1 + 4\pi M_s t_{\text{YIG}} \frac{\alpha_{\text{eff}}}{\hbar \gamma g_{\text{eff}}} \right) \times \gamma \mu_0 \left(H + \frac{M_{\text{eff}}}{2} \right), \quad (4)$$

where e is the elementary charge, θ_{SH} the spin Hall angle of Pt, α_{eff} the field dependent damping rate¹ taking into account inhomogenous broadening. Furthermore, g_{eff} denotes the effective spin mixing conductance,² which depends on the interface spin mixing conductance $g^{\uparrow\downarrow}$, the spin diffusion length l_s , thickness t_{Pt} , and electrical conductivity σ_{Pt} of Pt (see Ref. [26]). The variation of $I_{\text{crit}}^{\text{mod}}$ with the applied magnetic field taken from Ref. [10] is quantitatively well described by the theoretical model (dashed line). The small deviations for $\mu_0H \leq 20$ mT might be attributed to in-plane magnetocrystalline anisotropy fields [10]. We fit our data with Eq. (4), using $w_{\text{mod}} = 400$ nm, $M_s = 80$ kA m⁻¹ (from SQUID magnetometry measurements see Ref. [26]), $\theta_{\text{SH}} = 0.11$, $l_s = 1.5$ nm [35], and $\sigma_{\text{Pt}} = 2.15 \times 10^6 \Omega^{-1} \text{m}^{-1}$. Furthermore, we use the values of α_G and M_{eff} extracted from the FMR measurements. The spin mixing conductance $g^{\uparrow\downarrow}$ remains the only free fit parameter. We observe good quantitative agreement for large magnetic field magnitudes, but find a clear deviation for $\mu_0H < 40$ mT. However, if we assume $M_{\text{eff}} \approx 0$, the fit (solid line) corroborates our observed linear magnetic field dependence of $I_{\text{crit}}^{\text{mod}}$ in Fig. 4. Moreover, the linear dependence on μ_0H is in accordance with the results by Evelt *et al.*, who studied Bi:YIG thin films with PMA and nearly vanishing M_{eff} [24]. Fitting the data, we obtain $g^{\uparrow\downarrow} = (1.7 \pm 0.2) \times 10^{19}$ and $(9.9 \pm 0.4) \times 10^{18} \text{m}^{-2}$ in the limit of $M_{\text{eff}} = 0$, comparable to YIG/Pt structures on GGG [10]. Deviations between fit and data are potentially caused by uncertainties in the fixed parameters, as for example α_G and M_{eff} are determined from out-of-plane FMR. We can estimate the spin chemical potential, which is given by $\mu_s = [e\theta_{\text{SH}} I_{\text{dc}}^{\text{mod}} \tanh(\eta)]/[w_{\text{mod}} \sigma_{\text{Pt}} \eta]$ [32], at the threshold current $I_{\text{crit}}^{\text{mod}}$. Utilizing the device parameters from above, we calculate $\mu_s = 28.2$ meV for an applied magnetic field of $\mu_0H = 50$ mT, where we extracted a critical current of $I_{\text{crit}}^{\text{mod}} = 0.395$ mA (cf. Fig. 4). Similar values were found in our previous work [10].

In summary, we investigate magnon transport in YIG with strongly reduced M_{eff} induced via biaxial strain from growth on YSGG substrates [27]. Performing angle-dependent measurements in twin- and three-terminal devices, we find a

¹ $\alpha_{\text{eff}} = \alpha_G + \delta H(2\sqrt{H(H + M_{\text{eff}})})^{-1}$.

² $g_{\text{eff}} = [g^{\uparrow\downarrow} \frac{\hbar \sigma_{\text{Pt}}}{2e^2 l_s}] / [g^{\uparrow\downarrow} + \frac{\hbar \sigma_{\text{Pt}}}{2e^2 l_s}]$ and $\eta = t_{\text{Pt}}/(2l_s)$.

quantitatively similar behavior as observed for YIG films on GGG for small modulator currents I_{dc}^{mod} , while differences occur above the threshold value I_{crit}^{mod} when damping compensation is reached. Most importantly, we observe an increase of the magnon induced detector signal by a factor of about 6, which is much larger than reported previously [10]. Another important difference is the strictly linear field dependence of I_{crit}^{mod} . This interesting observation can be attributed to the nearly vanishing M_{eff} in our film confirming the expected

scaling of the threshold behavior with M_s and H_k . Our work provides an important step towards the detailed understanding of magnon transport in systems far from equilibrium and the basis for applications based on pure spin currents.

We gratefully acknowledge financial support from the Deutsche Forschungsgemeinschaft (DFG, German Research Foundation) under Germany's Excellence Strategy – EXC-2111 – 390814868 and project AL2110/2-1.

-
- [1] A. V. Chumak, V. I. Vasyuchka, A. A. Serga, and B. Hillebrands, Magnon spintronics, *Nat. Phys.* **11**, 453 (2015).
- [2] A. V. Chumak, A. A. Serga, and B. Hillebrands, Magnonic crystals for data processing, *J. Phys. D* **50**, 244001 (2017).
- [3] K. Nakata, P. Simon, and D. Loss, Spin currents and magnon dynamics in insulating magnets, *J. Phys. D* **50**, 114004 (2017).
- [4] L. J. Cornelissen, J. Liu, B. J. van Wees, and R. A. Duine, Spin-Current-Controlled Modulation of the Magnon Spin Conductance in a Three-Terminal Magnon Transistor, *Phys. Rev. Lett.* **120**, 097702 (2018).
- [5] V. Cherepanov, I. Kolokolov, and V. L'vov, The saga of YIG: Spectra, thermodynamics, interaction and relaxation of magnons in a complex magnet, *Phys. Rep.* **229**, 81 (1993).
- [6] Y. Kajiwara, K. Harii, S. Takahashi, J. Ohe, K. Uchida, M. Mizuguchi, H. Umezawa, H. Kawai, K. Ando, K. Takanashi, S. Maekawa, and E. Saitoh, Transmission of electrical signals by spin-wave interconversion in a magnetic insulator, *Nature (London)* **464**, 262 (2010).
- [7] L. J. Cornelissen, J. Liu, R. A. Duine, J. B. Youssef, and B. J. van Wees, Long-distance transport of magnon spin information in a magnetic insulator at room temperature, *Nat. Phys.* **11**, 1022 (2015).
- [8] H. Yu, O. d'Allivy Kelly, V. Cros, R. Bernard, P. Bortolotti, A. Anane, F. Brandl, F. Heimbach, and D. Grundler, Approaching soft x-ray wavelengths in nanomagnet-based microwave technology, *Nat. Commun.* **7**, 11255 (2016).
- [9] C. Liu, J. Chen, T. Liu, F. Heimbach, H. Yu, Y. Xiao, J. Hu, M. Liu, H. Chang, T. Stueckler, S. Tu, Y. Zhang, Y. Zhang, P. Gao, Z. Liao, D. Yu, K. Xia, n. Lei, W. ZHAO, and M. Wu, Long-distance propagation of short-wavelength spin waves, *Nat. Commun.* **9**, 738 (2018).
- [10] T. Wimmer, M. Althammer, L. Liensberger, N. Vlietstra, S. Geprägs, M. Weiler, R. Gross, and H. Huebl, Spin Transport in a Magnetic Insulator with Zero Effective Damping, *Phys. Rev. Lett.* **123**, 257201 (2019).
- [11] J. Gückelhorn, T. Wimmer, S. Geprägs, H. Huebl, R. Gross, and M. Althammer, Quantitative comparison of magnon transport experiments in three-terminal YIG/Pt nanostructures acquired via dc and ac detection techniques, *Appl. Phys. Lett.* **117**, 182401 (2020).
- [12] O. A. Santos, F. Feringa, K. S. Das, J. B. Youssef, and B. J. van Wees, Efficient Modulation of Magnon Conductivity in $Y_3Fe_5O_{12}$ using Anomalous Spin Hall Effect of a Permalloy Gate Electrode, *Phys. Rev. Appl.* **15**, 014038 (2021).
- [13] K. Ganzhorn, S. Klingler, T. Wimmer, S. Geprägs, R. Gross, H. Huebl, and S. T. B. Goennenwein, Magnon-based logic in a multi-terminal YIG/Pt nanostructure, *Appl. Phys. Lett.* **109**, 022405 (2016).
- [14] J. E. Hirsch, Spin Hall Effect, *Phys. Rev. Lett.* **83**, 1834 (1999).
- [15] M. I. Dyakonov and V. I. Perel, Possibility of orienting electron spins with current, *J. Exp. Theor. Phys. Lett.* **13**, 467 (1971).
- [16] S. T. B. Goennenwein, R. Schlitz, M. Pernpeintner, K. Ganzhorn, M. Althammer, R. Gross, and H. Huebl, Non-local magnetoresistance in YIG/Pt nanostructures, *Appl. Phys. Lett.* **107**, 172405 (2015).
- [17] S. Vélez, A. Bedoya-Pinto, W. Yan, L. E. Hueso, and F. Casanova, Competing effects at Pt/YIG interfaces: Spin hall magnetoresistance, magnon excitations, and magnetic frustration, *Phys. Rev. B* **94**, 174405 (2016).
- [18] B. L. Giles, Z. Yang, J. S. Jamison, and R. C. Myers, Long-range pure magnon spin diffusion observed in a nonlocal spin-seebeck geometry, *Phys. Rev. B* **92**, 224415 (2015).
- [19] J. Shan, L. J. Cornelissen, N. Vlietstra, J. Ben Youssef, T. Kuschel, R. A. Duine, and B. J. van Wees, Influence of yttrium iron garnet thickness and heater opacity on the nonlocal transport of electrically and thermally excited magnons, *Phys. Rev. B* **94**, 174437 (2016).
- [20] M. Althammer, Pure spin currents in magnetically ordered insulator/normal metal heterostructures, *J. Phys. D* **51**, 313001 (2018).
- [21] M. Althammer, All-electrical magnon transport experiments in magnetically ordered insulators, *Phys. Stat. Solid.* **15**, 2100130 (2021).
- [22] S. A. Bender, R. A. Duine, A. Brataas, and Y. Tserkovnyak, Dynamic phase diagram of dc-pumped magnon condensates, *Phys. Rev. B* **90**, 094409 (2014).
- [23] H. Suhl, The theory of ferromagnetic resonance at high signal powers, *J. Phys. Chem. Solids* **1**, 209 (1957).
- [24] M. Evelt, L. Soumah, A. B. Rinkevich, S. O. Demokritov, A. Anane, V. Cros, J. Ben Youssef, G. de Loubens, O. Klein, P. Bortolotti, and V. E. Demidov, Emission of Coherent Propagating Magnons by Insulator-Based Spin-Orbit-Torque Oscillators, *Phys. Rev. Appl.* **10**, 041002(R) (2018).
- [25] B. Divinskiy, S. Urazhdin, S. Demokritov, and V. Demidov, Controlled nonlinear magnetic damping in spin-hall nano-devices, *Nat. Commun.* **10**, 5211 (2019).
- [26] See Supplemental Material at <http://link.aps.org/supplemental/10.1103/PhysRevB.104.L180410>, which contains information on the sample fabrication, measurement procedure and a derivation of the used fitting functions for the critical modulator current. It contains Ref. [36].
- [27] C. Y. Guo, C. H. Wan, M. K. Zhao, H. Wu, C. Fang, Z. R. Yan, J. F. Feng, H. F. Liu, and X. F. Han, Spin-orbit torque switching in perpendicular $Y_3Fe_5O_{12}/Pt$ bilayer, *Appl. Phys. Lett.* **114**, 192409 (2019).

- [28] E. Popova, N. Keller, F. Gendron, L. Thomas, M.-C. Brianso, M. Guyot, M. Tessier, and S. S. P. Parkin, Perpendicular magnetic anisotropy in ultrathin yttrium iron garnet films prepared by pulsed laser deposition technique, *J. Vac. Sci. Technol. A* **19**, 2567 (2001).
- [29] H. Maier-Flaig, S. T. B. Goennenwein, R. Ohshima, M. Shiraishi, R. Gross, H. Huebl, and M. Weiler, Note: Derivative divide, a method for the analysis of broadband ferromagnetic resonance in the frequency domain, *Rev. Sci. Instrum.* **89**, 076101 (2018).
- [30] B. Hillebrands and A. Thiaville, *Spin Dynamics in Confined Magnetic Structures III* (Springer, Berlin, Heidelberg, 2006).
- [31] M. Collet, X. De Milly, O. d. Kelly, V. V. Naletov, R. Bernard, P. Bortolotti, J. B. Youssef, V. Demidov, S. Demokritov, J. L. Prieto, M. Munoz, V. Cros, A. Anane, G. de Loubens, and O. Klein, Generation of coherent spin-wave modes in yttrium iron garnet microdiscs by spin-orbit torque, *Nat. Commun.* **7**, 10377 (2016).
- [32] L. J. Cornelissen, K. J. H. Peters, G. E. W. Bauer, R. A. Duine, and B. J. van Wees, Magnon spin transport driven by the magnon chemical potential in a magnetic insulator, *Phys. Rev. B* **94**, 014412 (2016).
- [33] S. Takei, Spin transport in an electrically driven magnon gas near Bose-Einstein condensation: Hartree-Fock-Keldysh theory, *Phys. Rev. B* **100**, 134440 (2019).
- [34] H. Ulrichs, From chaotic spin dynamics to noncollinear spin textures in YIG nanofilms by spin-current injection, *Phys. Rev. B* **102**, 174428 (2020).
- [35] M. Althammer, S. Meyer, H. Nakayama, M. Schreier, S. Altmannshofer, M. Weiler, H. Huebl, S. Geprägs, M. Opel, R. Gross, D. Meier, C. Klewe, T. Kuschel, J.-M. Schmalhorst, G. Reiss, L. Shen, A. Gupta, Y.-T. Chen, G. E. W. Bauer, E. Saitoh *et al.*, Quantitative study of the spin Hall magnetoresistance in ferromagnetic insulator/normal metal hybrids, *Phys. Rev. B* **87**, 224401 (2013).
- [36] W. Zhang, W. Han, X. Jiang, S.-H. Yang, and S. Parkin, Role of transparency of platinum-ferromagnet interface in determining intrinsic magnitude of spin hall effect, *Nat. Phys.* **11**, 496 (2015).